

Three-dimensional modelling of accretion columns: spatial asymmetry and self-consistent simulations

M. I. Gornostaev^{1,2}★

¹ Sternberg Astronomical Institute, Lomonosov Moscow State University, Universitetskij pr., 13, Moscow 119234, Russia

² Faculty of Physics, Lomonosov Moscow State University, Leninskie Gory, 1, Moscow 119991, Russia

Accepted XXX. Received YYY; in original form ZZZ

ABSTRACT

The paper presents the results of three-dimensional (3D) modelling of the structure and the emission of accretion columns formed above the surface of accreting strongly magnetized neutron stars under the circumstances when a pressure of the photons generated in the column base is enough to determine the dynamics of the plasma flow. On the foundation of numerical radiation hydrodynamic simulations, several 3D models of accretion column are constructed. The first group of the models contains spatially 3D columns. The corresponding calculations lead to the distributions of the radiation flux over the sidewalls of the columns which are not characterized by axial symmetry. The second group includes the self-consistent modelling of spectral radiative transfer and two-dimensional spatial structure of the column, with both thermal and bulk Comptonization taken into account. The changes in the structure of the column and the shape of X-ray continuum are investigated depending on physical parameters of the model.

Key words: accretion – radiation: dynamics – radiative transfer – scattering – shock waves – X-rays: binaries

1 INTRODUCTION

The location of the emitting regions of accreting strongly magnetized neutron stars is controlled by the magnetic field, which is often assumed to be dipole in solving the problems. If the axis of a dipole does not pass through the neutron star centre, the modelling of an emitting structure cannot be performed under the assumption of axial symmetry of the problem, which is three-dimensional (3D) in this case. The same is rightful when the accretion channel near the neutron star surface has a transverse section of comparatively complicated form. These are the reasons for considering 3D models of radiation-dominated accretion columns, whose two-dimensional (2D) structures were calculated earlier (Davidson 1973, Wang & Frank 1981, Postnov et al. 2015). The numerical solutions presented below give the impression of the quantitative deviation of the shock form from the 2D axially symmetric one and lead to the 2D distributions of radiative flux over the column sidewall. The consequences of the presented consideration can be useful for the investigation of properties of spatially one-dimensional (1D) solutions (Becker & Wolff 2007, Farinelli et al. 2012, Farinelli et al. 2016, West, Wolfram & Becker 2017a,b), as well as for the modelling and interpretation of the observed pulse profiles of X-ray pulsars emission.

Another kind of 3D problems is related with a transition to simultaneous modelling of the dynamics of the matter and radia-

tive transfer. The solution procedure offered does not involve the frequency-integrated energy equation. One can notice this immediately comparing the results of Section 2, where spatially 3D computations are described, with the results of Section 3, devoted to the modelling of spatially 2D radiation-dominated shocks with simultaneous calculation of spectral radiation energy density at each point of the column. Thus, hereafter a self-consistent solution will be understood as a set of functions that are a solution of one and the same system of equations and describe the velocity of the plasma flow, the electron temperature distribution and the radiation spectrum within a column.

Both approaches are based, first of all, on the assumption that the matter flow satisfies the hydrodynamic limit. The Compton scattering is considered as the main process of the energy exchange between the plasma and the radiation field. The basic equations under consideration describe the propagation of the radiation not only along the magnetic field but also in transverse directions, governing the mound-like structure of the shock and determining the corresponding distributions of the radiation flux over the column sidewall.

Section 4 contains some remarks and conclusions.

★ E-mail: mgornost@gmail.com

2 THREE-DIMENSIONAL RADIATION-DOMINATED SHOCKS

2.1 The relations between main equations

Under the circumstances of the radiation-dominated accretion columns, the structure formed above the magnetic poles has a significant optical depth to the Thomson scattering, and the radiative pressure is much higher here than the gas one. These things allow to believe that the diffusion approximation is applicable to describe the radiative transfer, and that the pressure tensor is isotropic. In all frames considered below, the neutron star is at rest. Then, the radiation flux within the column can be written as

$$\mathbf{F} = -D\nabla u + \frac{4}{3}u\mathbf{v}, \quad (1)$$

and the momentum equation has the form

$$n_e m_p (\mathbf{v} \cdot \nabla) \mathbf{v} = -\frac{1}{3} \nabla u, \quad (2)$$

where u denotes the frequency-integrated radiation energy density, \mathbf{v} is the bulk velocity of the matter, n_e is the electron number density, m_p is the proton mass, and D is the diffusion coefficient. The gravitation and the gas pressure are neglected in the equation (2). The considered physical situation, satisfying the limit $p_g/p_r \ll 1$, where p_g and p_r denote the gas pressure and the radiation one, respectively, allows one not only to set $p = p_r = u/3$ in eq. (2), but also not to consider further the equations of state for both electron and ion gas components.

Let us assume that magnetic field is uniform inside the computational domains. The velocity vector will be supposed to be collinear to the magnetic field vector, which corresponds to situation when the matter is confined in the transverse directions by a magnetic field whose pressure far exceeds any other within the problem. The stationary continuity equation then reads as

$$n_e m_p v = S, \quad (3)$$

where $v = |\mathbf{v}|$, $S = \dot{M}/A$, with \dot{M} is the mass accretion rate per one neutron star magnetic pole and A is a column transverse section area. The integration of eq. (2) yields

$$v = v_0 - \frac{u}{3S}. \quad (4)$$

Here, v_0 is the absolute value of the velocity at a height, where one can set $u = 0$ (far above the neutron star surface).

The stationary equation for the frequency-integrated radiation energy density (Blandford & Payne 1981) has the form

$$\nabla \cdot (D\nabla u) - \mathbf{v} \cdot \nabla u - \frac{4}{3}u\nabla \cdot \mathbf{v} + \frac{un_e\sigma_T}{m_e c} (4kT_e - \langle \epsilon \rangle) = 0, \quad (5)$$

where k is the Boltzmann constant, m_e is the electron mass, T_e is the electron temperature, the scattering cross-section is set to be equal to the Thomson value, σ_T , and the mean (energy-weighted) value $\langle \epsilon \rangle$ of the photon energy, ϵ , is related with angle-averaged photon occupation number n as follows,

$$\langle \epsilon \rangle = \frac{\int \epsilon^4 n d\epsilon}{\int \epsilon^3 n d\epsilon}. \quad (6)$$

After substituting in eq. (5) the temperature (Zel'dovich & Levich 1970)

$$T_e = \frac{1}{4k} \frac{\int \epsilon^4 n d\epsilon}{\int \epsilon^3 n d\epsilon} \quad (7)$$

which is equal to the electron one in the approximation of

the local Compton equilibrium, the term corresponding to the energy-integrated Kompaneets operator (Kompaneets 1956) becomes equal to zero, so that

$$\nabla \cdot (D\nabla u) - \frac{4}{3}u\nabla \cdot \mathbf{v} - \mathbf{v} \cdot \nabla u = 0. \quad (8)$$

The term n^2 is neglected in expression (7). From eq. (8) it follows that

$$\nabla \cdot \left(-D\nabla u + \frac{4}{3}u\mathbf{v} \right) = \frac{1}{3}\mathbf{v} \cdot \nabla u, \quad (9)$$

and thus the energy equation can be written as

$$\nabla \cdot \mathbf{F} = -n_e m_p \mathbf{v} \cdot \nabla \left(\frac{v^2}{2} \right). \quad (10)$$

Previous (two-dimensional) calculations are based on the solution of the energy equation of type of equation (10) making use of the velocity value determined by momentum equation and taking into account the continuity equation (Davidson 1973 and references to this work). The denoted relation between equations (5) and (10) plays a determinative role for constructing the solutions, presented in Section 3.

2.2 Geometry

It is reasonable to carry out spatially 3D calculations in Cartesian coordinates. Let us introduce them in such a way that the axis z will have the direction opposite to the velocity of the flow. Let the idealized neutron star surface being approximated by the plane inside the computational domains intersect the xy plane, and let α denote the angle between these planes ($\alpha < \pi/2$). Meanwhile, let the neutron star surface intersect the z axis in the half-space $z > 0$.

Two kinds of column geometry are considered numerically in the current section.

Cylindrical filled column. Consider the column in the model of circle truncated cylinder with radius r_0 , the continuity equation includes the area $A = \pi r_0^2$ in this case. Let the axis of the cylinder be superposed with the z axis, and the straight line originated by the intersection of the xy plane and neutron star surface be the tangent to the cylinder sidewall at the point $x = r_0$, $y = 0$, $z = 0$.

The value of r_0 being determined by the Alfvén radius r_A ,

$$r_0 = \beta r_{ns} \sqrt{\frac{r_{ns}}{r_A}}, \quad (11)$$

where r_{ns} is the neutron star radius, is not defined strictly since the factor $\beta \sim 1$ depends on the freezing depth of the accreted plasma in the magnetosphere and the geometry of the accretion flow beyond the Alfvén surface.

Unclosed hollow column. On the base of descriptions of possible accretion column geometry (Basko & Sunyaev 1976, Meszaros 1984, Mushtukov et al. 2015, Postnov et al. 2015), in the present work the modelling has been carried out also for another case. This last corresponds to the arch-like form of the channel transverse section and is realized in the frame of consideration of two circle cylinders with the axes parallel to the z axis. Namely, let the axis of cylinder of radius r_0 be superposed with the z axis, and the axis of cylinder of radius $r_0 + br_0$ intersect the xy plane at the point $x = s$, $y = 0$, with $br_0 < s < (2 + b)r_0$. Then the directrices of cylinders lying in the same plane intersect at two points with the same abscissa x^* . Consider the arcs lying on the same side of the chord passing through the intersection points in the case of $x^* < 0$. For the definiteness let us choose two longer

arcs and consider the figure enclosed between them. Thus, the column sidewalls are generated by the generatrices of cylinders crossing these arcs, and the continuity equation (3) includes in considering case the area A of specified figure. It can be calculated as a difference between areas of two corresponding circle segments:

$A = A_2 - A_1$, where $A_1 = \frac{r_0^2}{2}(\psi_1 - \sin \psi_1)$, $A_2 = \frac{(r_0 + br_0)^2}{2}(\psi_2 - \sin \psi_2)$, with $\psi_1 = 2 \arccos\left(\frac{x^*}{r_0}\right)$, $\psi_2 = 2 \arccos\left(\frac{x^* - s}{r_0 + br_0}\right)$. The straight originated by the intersection of the xy plane and neutron star surface will be the tangent to column sidewall at the point $x = r_0 + br_0$, $y = 0$, $z = 0$.

The modelling is feasible as well in the geometry of closed hollow columns (when $|s| \leq br_0$, and $A = (2 + b)b\pi r_0^2$). The case of $s = 0$ and $\alpha = 0$ corresponds to 2D problem of ring-kind geometry, considered numerically by Postnov et al. (2015). The numerical consideration of so-called spaghetti-like geometry (Meszaros 1984) can be reduced to the modelling of a set of radiation-dominated columns while the approach described above is applicable.

2.3 Computations

Let us now describe the solution of the system of equations containing (1), (3), (4) and (10), and coming to the one partial differential equation of the elliptic type.

The transition to the dimensionless variables is performed by the changes:

$$\tilde{x} = \frac{\sigma_T S}{m_p c} x, \quad \tilde{y} = \frac{\sigma_T S}{m_p c} y, \quad \tilde{z} = \frac{\sigma_T S}{m_p c} z, \quad Q = \frac{v^2}{v_0^2}, \quad (12)$$

where c is the speed of light, and v_0 being now specified equals to the free-fall velocity at the upper boundary,

$$v_0 = \sqrt{\frac{2GM_{\text{ns}}}{r_{\text{ns}} + z_0}}, \quad (13)$$

with G is the gravitation constant, z_0 is the coordinate of the upper boundary; hereafter, it is set that $r_{\text{ns}} = 10^6$ cm and the neutron star mass $M_{\text{ns}} = 1.5M_\odot$.

The question of the specific form of the diffusion coefficient was not considered above. Its definition is related with the method of the describing of scattering in the strong magnetic field used by Wang & Frank (1981), Becker & Wolff (2007), West et al. (2017a). This modification of the grey approximation is aimed at the effective accounting on the radiative transfer of the angular and frequency dependence of scattering cross-sections for ordinary and extraordinary modes.

The approximation is constructed by analyzing the frequency dependence of non-relativistic scattering cross-sections derived by Canuto, Lodenquai & Ruderman (1971). One can consider two narrow ranges of the angle θ of the initial direction of the wavevector with respect to the magnetic field vector. Let the condition $\epsilon \gtrsim h\nu_L$ be satisfied, where ν_L is the plasma frequency and h is the Planck constant. For θ that are close to 0, the cross-sections read as (Canuto et al. 1971, Lodenquai et al. 1974)

$$\sigma_j \simeq \sigma_T \left(\frac{\epsilon^2}{(\epsilon + (-1)^j \epsilon_B)^2} + \frac{1}{2} \sin^2 \theta \right), \quad (14)$$

where the cyclotron energy $\epsilon_B = \hbar e B / (2\pi m_e c)$, e is the elementary charge, $j = 1$ for the extraordinary mode, and $j = 2$ for the ordinary one. For θ that are close to $\pi/2$,

$$\sigma_1 \simeq \sigma_T \left(\frac{\epsilon^2}{(\epsilon - \epsilon_B)^2} + \cos^2 \theta \right), \quad (15)$$

$$\sigma_2 = \sigma_T \sin^2 \theta.$$

It can be seen from these expressions that while, for $\epsilon \ll \epsilon_B$, $\sigma_1 \simeq \sigma_T(\epsilon/\epsilon_B)^2$ in both directions, $\sigma_2 \simeq \sigma_T$ in the perpendicular direction and $\sigma_2 \simeq \sigma_T(\epsilon/\epsilon_B)^2$ in the parallel one; for $\epsilon \gg \epsilon_B$, $\sigma_j = \sigma_T$, $j = 1, 2$. From here one can see the anisotropic character of the scattering in the highly magnetized plasma, the effective account of which is based thus on the judicious parametrisation of the value of ratio $(\epsilon^*/\epsilon_B)^2$, where the mean energy $\epsilon^* < \epsilon_B$ (Wang & Frank 1981) replaces its specific value ϵ . Thus, the main components of the diffusion tensor, describing the propagation of photons across and along the magnetic field, are taken to be equal to

$$D^\perp = \frac{c}{3\sigma_T n_e} \quad (16)$$

and

$$D^\parallel = \left(\frac{\epsilon_B}{\epsilon^*} \right)^2 D^\perp, \quad (17)$$

respectively. In the calculations it is set that $(\epsilon_B/\epsilon^*)^2 = 10$, excepting two cases described in the next section.

Notwithstanding the huge values of the scattering cross-sections on the cyclotron resonance, the radiation pressure force distinguishes significantly from its values in the case of non-magnetized atmosphere, as Gnedin & Nagel (1984) showed, only in superficial layers (the plane homogeneous hot magnetized atmosphere was being investigated). It is possible to believe, consequently, that the cyclotron photons are not able to influence the dynamics of the flow dramatically.

The specific value of magnetic field strength is not involved explicitly in the scattering cross-sections under the current consideration. Therefore, the values of r_0 and D^\parallel will be varied independently.

Turning now to the equations (1), (3), (4), and (10), after the substitutions one can write in the dimensionless form the following equation:

$$\frac{\partial^2 Q}{\partial \tilde{x}^2} + \frac{\partial^2 Q}{\partial \tilde{y}^2} + \frac{D_\parallel}{D_\perp} \frac{\partial^2 Q}{\partial \tilde{z}^2} - \frac{\partial}{\partial \tilde{z}} (8\sqrt{Q} - 7Q) = 0. \quad (18)$$

The numerical solution of this equation is carried out by the time relaxation method, which consists in searching the stationary solution of the problem for parabolic equation including the same spatial operator as the original elliptic equation. The difference schemes are explicit, and the rectangular equidistant meshes are used. The second derivatives are approximated by central three-point finite-difference patterns, and the first derivatives are approximated by central differences. All the calculations described in the current and next sections are performed using the programs written in C language, the computer based on Intel Core i9-9900KF CPU is exploited.

Since the main fraction of the kinetic energy of the matter transforms into the radiation energy in the shock, near the star surface the appropriate condition is $Q = 0$, which leads to the infinite density of the matter at this boundary (the neutron star surface is impenetrable for the matter flow). For numerical reasons, it can be assumed that the radiation energy density at the bottom boundary is slightly (1–3 %) less than the maximal value $3Sv_0$. At the upper boundary, it is set that $Q = 1$. The value of z_0 is chosen enough to be affected on the solution for the shock structure. The radiation leaves the column and emerges to the surrounding space freely, so that in dependence on required accuracy, one can use the condition

$$Q = 1, \quad (19)$$

or the condition for the projection of the radiation flux vector onto

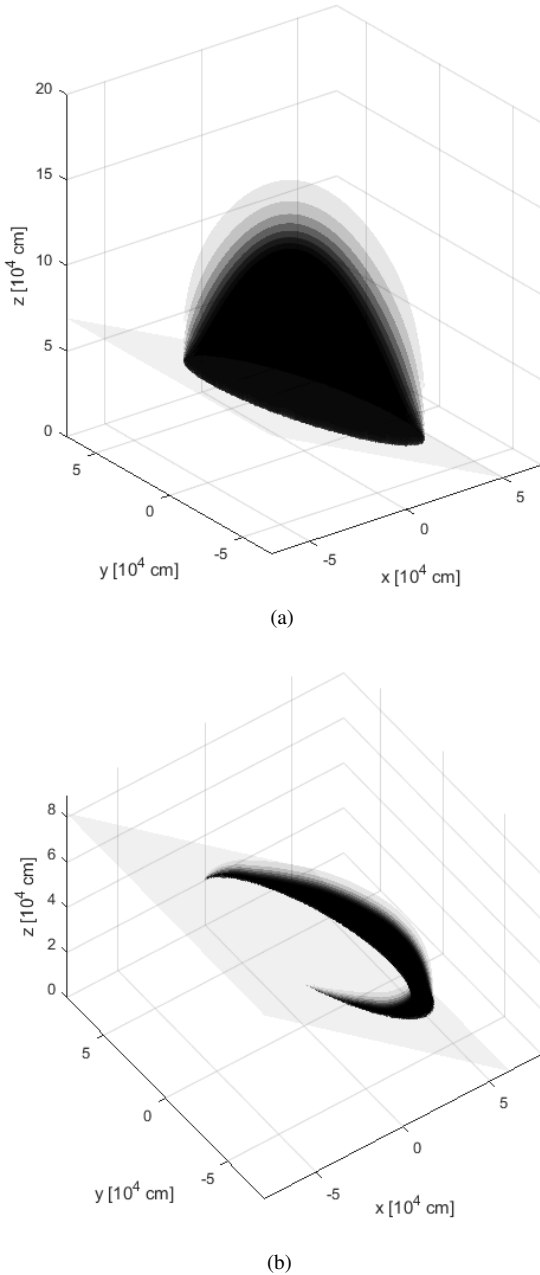


Figure 1. Three-dimensional structure of the radiation-dominated column simulated in the geometry of the filled truncated cylinder (a) and unclosed narrow circlet (b). The level surfaces of quantity Q (0.9, 0.8, ...) are shown for $\alpha = 30^\circ$, the other parameters are specified in the main text. The neutron star surface is represented by the grey plane.

the direction of a normal unit vector \mathbf{n} to the outer side of column surface,

$$F_n = \kappa c u. \quad (20)$$

Here, $\kappa = \text{const} \lesssim 1$, and $F_n = -D \frac{\partial u}{\partial n}$, where $\frac{\partial u}{\partial n}$ is a directional derivative of u in the \mathbf{n} direction. For computational reasons, the condition (20) is realized at the side surfaces of the unclosed hollow column, and the condition (20) with $\kappa = 2/3$ is set in the model of the filled column. The numerical realization of boundary condition (20) is performed making use of the forward or backward

(in dependence on coordinate quarter) three-point finite-difference patterns approximating the first derivatives.

2.4 Results

The examples of 3D structures of accretion columns obtained by solving equation (18) are shown in Fig. 1. The structure of the filled column is displayed in Fig. 1a, where the set of surfaces of equal quantity Q is plotted. For the specific computation, the following values of the parameters are used: the mass accretion rate $\dot{M}_{17} = \dot{M}/(10^{17} \text{ g s}^{-1}) = 1$, the inclination angle $\alpha = 30^\circ$, and the column radius $r_0 = 5 \times 10^4 \text{ cm}$.

Fig. 1b shows the level surfaces of Q obtained due to numerical simulations in unclosed hollow column geometry for the same set of parameters, with $b = 0.1$ and $s = 0.15r_0$. The code provides, in principle, the arbitrary spatial orientation of the emitting region.

Two-dimensional slices of the column structure in the xz plane are shown in Fig. 2. They demonstrate graphically the extent of asymmetry of solutions in the case of the filled column (Fig. 2a) and hollow unclosed column (Fig. 2b).

Fig. 3 shows calculated in the xz plane distributions of the modulus of the dimensionless component of the radiation flux $\tilde{F}_x = F_x/(Sv_0^2/2) = \partial Q/\partial \tilde{x}$ along the column sidewall. In the figures, z_{ns} denotes the vertical coordinate of the neutron star surface at current x and y . At fixed \dot{M} and A , the solution for Q does not depend on v_0 when the first-type boundary condition (19) is set at the side surface. Therefore, it is useful to represent the radiation flux in units of $Sv_0^2/2$. Since $D^\perp \propto v_0 \sqrt{Q}$, the realization of conditions of the type (20) at the side boundary introduces the dependence of the solution on v_0 . The variation of v_0 in the common-sense ranges entails the slight change of the shock width near the column sidewall.

The quantities

$$f(\alpha) = \frac{\int |F_x(-r_0, 0, z, \alpha)| dz}{\int F_x(r_0, 0, z, \alpha) dz} \quad (21)$$

for the filled column and

$$f'(\alpha) = \frac{\int |F_x(r_0, 0, z, \alpha)| dz}{\int F_x(r_0 + br_0, 0, z, \alpha) dz} \quad (22)$$

in the circlet-like geometry may be considered as the measures of the azimuthal anisotropy of the column emission in the dependence on the angle value at fixed accretion rate and *ceteris paribus*. For the presented calculations, the particular values are $f(15^\circ) \simeq 0.81$, $f(30^\circ) \simeq 0.59$, $f'(15^\circ) \simeq 0.76$, and $f'(30^\circ) \simeq 0.60$. In the case of the boundary condition (19), when the quantity Q at the sidewalls does not depend on the height, the emergent flux is calculated at the internal nodes of the grid closest to the boundary nodes (without using the latter). This allows to avoid distortions near the base of the column: in the immediate vicinity of the boundary, the radiation energy density behaves qualitatively as if condition of type (20) were specified there.

It is possible to define similar relations through the integral emission of the column sidewalls. Let Γ_1 and Γ_2 be the sections of the filled column sidewall that are separated by the yz plane and thus lie in different half-spaces, $x < 0$ and $x > 0$, respectively. Moreover, let Σ_1 denote the surface of the interior sidewall of the hollow column (corresponding to the radius r_0) and Σ_2 , the surface of the outer one. Then, the ratio of the luminosities of the specified surfaces in each case will read as

$$\ell(\alpha) = \frac{\iint_{\Gamma_1} F_n(x, y, z, \alpha) d\Gamma_1}{\iint_{\Gamma_2} F_n(x, y, z, \alpha) d\Gamma_2} \quad (23)$$

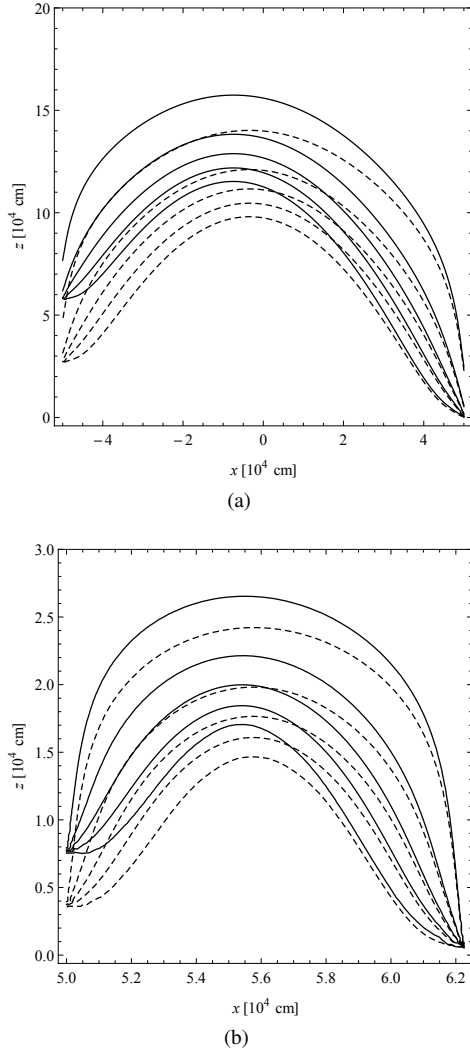


Figure 2. Two-dimensional slices of the 3D structure of the shocks in the xz plane: the filled column (a) and unclosed hollow column (b). The contours of Q are shown from 0.9 to 0.1 (from top to bottom) with interval 0.2 for $\alpha = 15^\circ$ (dashed lines) and $\alpha = 30^\circ$ (solid lines).

and

$$\ell'(\alpha) = \frac{\iint_{\Sigma_1} F_n(x, y, z, \alpha) d\Sigma_1}{\iint_{\Sigma_2} F_n(x, y, z, \alpha) d\Sigma_2}. \quad (24)$$

In all expressions (21)–(24) the dependence of the flux component on the angle α should be understood as the dependence on the problem parameter determining the geometry of the computational area and affecting the solution.

The calculations give $\ell(15^\circ) \simeq 0.92$, $\ell(30^\circ) \simeq 0.83$, $\ell'(15^\circ) \simeq 0.95$ and $\ell'(30^\circ) \simeq 0.87$. Fig. 4 displays 2D distributions of \tilde{F}_n (normalization is prior) over the column surface. The angular coordinate λ is the azimuthal angle counted in the xy plane. The panels in Fig. 4b do not show the regions with $\lambda > 115^\circ$ where the channel is too thin to linger the radiation in the medium long enough and stop the flow at a significant height: here the plasma falls freely nearly to the neutron star surface causing almost zero diffusion flux from the side boundary.

The solutions illustrate the importance of taking into account the radiation diffusion across the magnetic field, accompanied by

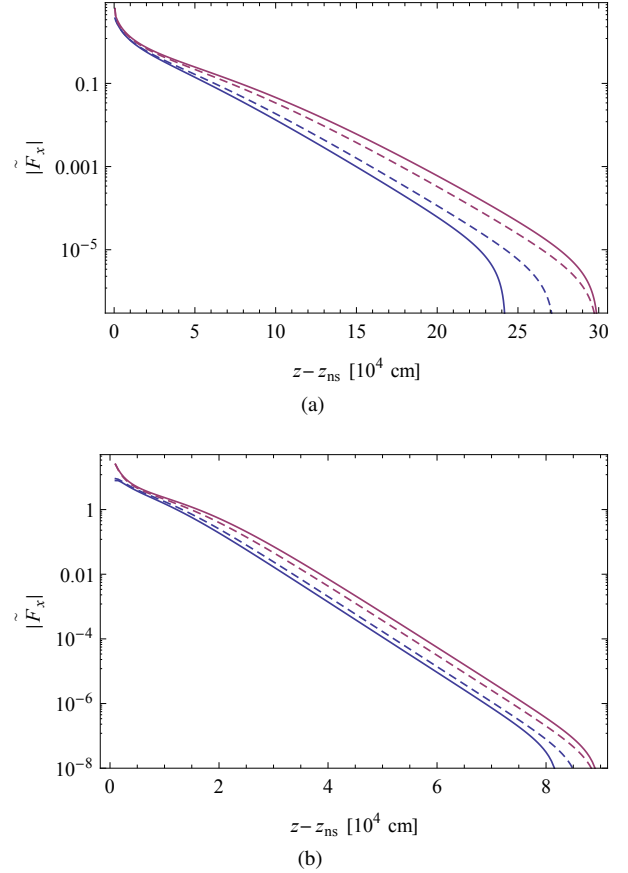


Figure 3. The modulus of dimensionless component \tilde{F}_x of radiative flux (1) plotted against the height $z - z_{\text{ns}}$ above the neutron star surface in the xz plane for the filled (a) and unclosed hollow (b) column. The dependencies are shown for $\alpha = 15^\circ$ (dashed lines) and $\alpha = 30^\circ$ (solid lines). Two lower lines correspond to the left boundaries, and two upper ones, to the right boundaries of 2D slices (see Fig. 2).

the process of advection in the vertical direction. The main contribution to the luminosity is caused by the photons coming from the side surface of the column not very far from neutron star surface and forming a fan beam. The investigation of the properties of observed pulse profiles is a problem deserving a separate consideration. To compare theoretical results with observational data and construct the conclusions concerning the influence of spatial asymmetry, one should take into account the angular distribution of the sidewall emission which is directed mainly towards the neutron star surface. The questions of the emergent radiation spectra and the distribution of spectral radiation flux over the column surface will be considered in the grey approximation in the following section.

3 THE PHOTON ENERGY AS A THIRD COORDINATE

3.1 The equations and boundary conditions

The spatial and time evolution of the angle-averaged photon occupation number in the moving compressible medium can be described in the diffusion approximation by the kinetic equation

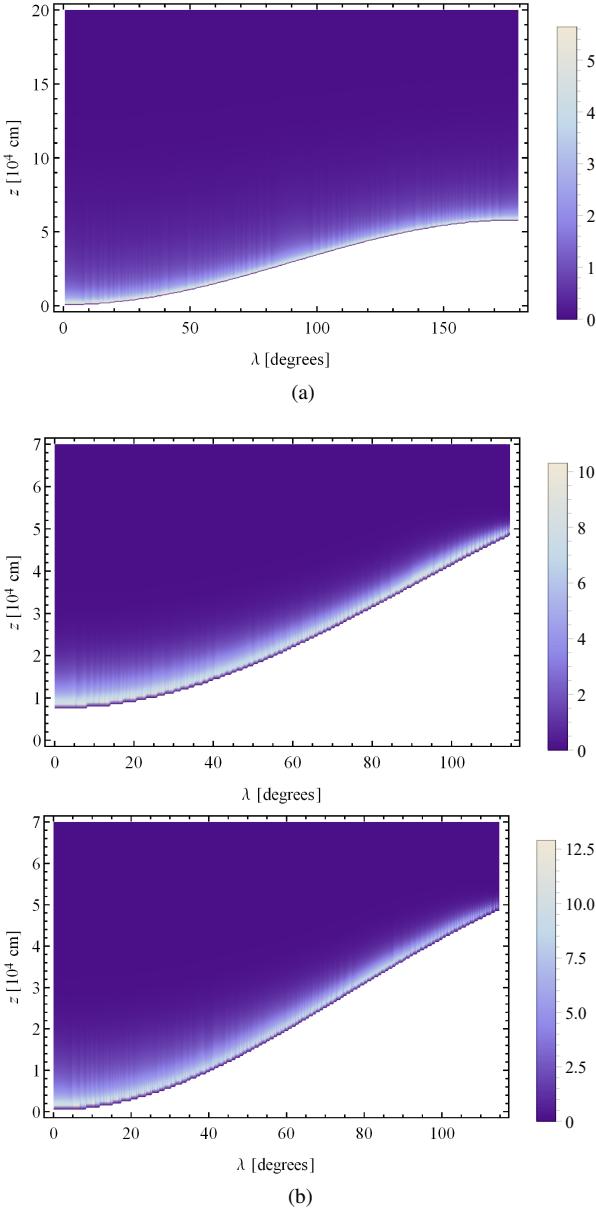


Figure 4. The distributions of the normal component of radiation flux \tilde{F}_n over the column sidewalls for the filled (a) and unclosed hollow (b) geometry, $\alpha = 30^\circ$. The upper of the panels (b) corresponds to the inner sidewall, and the bottom panel, to the outer one.

(Blandford & Payne 1981, Lyubarskii & Syunyaev 1982)

$$\nabla \cdot (D \nabla n) - \mathbf{v} \cdot \nabla n + \frac{n_e \sigma_T}{m_e c \epsilon^2} \frac{\partial}{\partial \epsilon} \left[\epsilon^4 \left(n + k T_e \frac{\partial n}{\partial \epsilon} \right) \right] + \nabla \cdot \mathbf{v} \frac{\epsilon}{3} \frac{\partial n}{\partial \epsilon} = \frac{\partial n}{\partial t}, \quad (25)$$

from which equation (5) and, as a consequence, equation (18) are derived. Equation (25) takes into account the diffusion, advection, and thermal and bulk Comptonization. To describe the thermal Comptonization in strongly magnetized plasma, the mean cross-section $\langle \sigma \rangle$ determined by the cross-sections along and across the magnetic field can be introduced (Becker & Wolff 2007).

Now consider the axially symmetric filled column in the model of circle cylinder. Introducing cylindrical coordinates cen-

tred at the axis of the cylinder so that the z axis is again directed towards the flow and $z = 0$ at the neutron star surface, let us now solve in these coordinates the system including eq. (25), that turns out to be 3D in the $r z \epsilon$ space, instead of equation (10). Thus the problem is to solve the stationary system of equations (25), (2), (3), (7) ($\partial n / \partial t = 0$), which is reduced to the system (25), (4), (7) when the gravitation is neglected (the present case).

The velocity (4) is determined making use of the quantity $u = \int u_\epsilon d\epsilon$, where $u_\epsilon = 8\pi\epsilon^3 n / (c^3 h^3)$. The expression for the temperature (7) is a consequence of solving the Fokker–Planck equation for thermal electrons having a stationary distribution function and interacting with non-equilibrium radiation which is assumed to be isotropic.

At the upper boundary, at the height $z = z_0$, the velocity component $v_z = -v$ is determined by the free-fall velocity value,

$$v_z(r, z_0) = -v_0. \quad (26)$$

The components of the spectral radiation flux are written as follows:

$$F_{\epsilon, r} = -D^\perp \frac{\partial u_\epsilon}{\partial r}, \quad (27)$$

$$F_{\epsilon, z} = -D^\parallel \frac{\partial u_\epsilon}{\partial z} + v_z u_\epsilon - \frac{v_z \epsilon}{3} \frac{\partial u_\epsilon}{\partial \epsilon}. \quad (28)$$

Free escape of the photons from the column leads again to the following condition at the sidewall:

$$F_{\epsilon, r}(r_0, z) = \frac{2}{3} c u_\epsilon(r_0, z). \quad (29)$$

Since the solution of the momentum equation is written under the condition $u(r, z_0) = 0$, at the upper boundary it is reasonable to set

$$u_\epsilon(r, z_0) = 0. \quad (30)$$

The condition $-D^\parallel \frac{\partial u_\epsilon}{\partial z} = \frac{2}{3} c u_\epsilon$ is also appropriate and becomes equivalent to condition (30) far above the shock, where the velocity is approximately constant. At the central axis

$$\frac{\partial u_\epsilon(0, z)}{\partial r} = 0. \quad (31)$$

The physical meaning of these relations corresponds to their frequency-integrated analogues. At the bottom boundary, the approximate condition $u(r, 0) = 3S v_0$ is used, which means that $v(r, 0) = 0$. Then at this boundary one can set

$$a T_0^4 = u(r, 0), \quad (32)$$

where $a = 8\pi^5 k^4 / (15 h^3 c^3)$ is the radiation constant. Determining from here T_0 one can suppose the blackbody bottom boundary condition for spectral radiation energy density:

$$u_\epsilon(r, 0) = \frac{8\pi\epsilon^3}{c^3 h^3} \frac{1}{\exp\left(\frac{\epsilon}{k T_0}\right) - 1}. \quad (33)$$

It is also assumed (Farinelli et al. 2012) that there are no photons at the boundaries of the photon energy grid, $\epsilon_1 = 0.1$ keV and $\epsilon_2 = 500$ keV, so that

$$u_\epsilon(\epsilon_1) = u_\epsilon(\epsilon_2) = 0. \quad (34)$$

3.2 Computations

The stationary solution of the system described above is constructed by the iterative procedure based on the time relaxation method. At each time-step, the electron temperature, velocity, and

spectral radiation energy density are determined alternatively by expressions (7), (4), and from eq. (25), respectively. As the initial distribution of the spectral radiation energy density, the blackbody spectrum with temperature 0.1 keV is used.

To realize the numerical modelling, it is reasonable to introduce the new variables. Using the logarithmic scale, let us determine the photon energy as the function of the dimensionless variable ξ , so that $\epsilon = \epsilon_0 e^\xi$, where $\epsilon_0 = 1$ keV. Then, the spectral radiation energy density per unit of ξ is equal to

$$u_\xi = u_\epsilon \frac{d\epsilon}{d\xi} = \frac{8\pi\epsilon_0^4 e^{4\xi}}{c^3 h^3} n. \quad (35)$$

For computational reasons, it is convenient to write the equations for the function $\tilde{u}_\xi = e^{4\xi} n$. The dimensionless variables are now defined by the relations:

$$\begin{aligned} \tilde{r} &= \frac{r}{R_0}, \quad \tilde{z} = \frac{z}{R_0}, \quad R_0 = 10^4 \text{ cm}; \\ \tilde{v}_z &= \frac{v_z}{v_0}, \quad \theta = \frac{kT_e}{\epsilon_0}, \quad \tilde{t} = \frac{t}{t_0}, \quad t_0 = \frac{\sigma_T \dot{M} R_0^2}{v_0 c m_p \pi r_0^2}. \end{aligned} \quad (36)$$

In terms of these variables eq. (25) can be written as follows:

$$\begin{aligned} & \frac{1}{\tilde{r}} \frac{\partial}{\partial \tilde{r}} \left(\tilde{r} \tilde{D}^\perp \frac{\partial \tilde{u}_\xi}{\partial \tilde{r}} \right) + \frac{\partial}{\partial \tilde{z}} \left(\tilde{D}^\parallel \frac{\partial \tilde{u}_\xi}{\partial \tilde{z}} \right) - \frac{v_0 t_0}{R_0} \tilde{v}_z \frac{\partial \tilde{u}_\xi}{\partial \tilde{z}} \\ & + \frac{t_0 f_0 \langle \tilde{\sigma} \rangle}{|\tilde{v}_z|} \theta \frac{\partial^2 \tilde{u}_\xi}{\partial \tilde{\xi}^2} + \left(\frac{1}{3} \frac{v_0 t_0}{R_0} \frac{\partial \tilde{v}_z}{\partial \tilde{z}} + \frac{t_0 f_0 \langle \tilde{\sigma} \rangle}{|\tilde{v}_z|} (e^\xi - 5\theta) \right) \frac{\partial \tilde{u}_\xi}{\partial \tilde{\xi}} \\ & + \left(\frac{t_0 f_0 \langle \tilde{\sigma} \rangle}{|\tilde{v}_z|} 4\theta - \frac{4}{3} \frac{v_0 t_0}{R_0} \frac{\partial \tilde{v}_z}{\partial \tilde{z}} \right) \tilde{u}_\xi = \frac{\partial \tilde{u}_\xi}{\partial \tilde{t}}. \end{aligned} \quad (37)$$

Here,

$$\begin{aligned} \tilde{D}^{\perp,\parallel} &= \frac{t_0}{R_0^2} D^{\perp,\parallel}, \quad \langle \tilde{\sigma} \rangle = \frac{\langle \sigma \rangle}{\sigma_T} = \sqrt{\frac{D^\perp}{D^\parallel}}, \\ \phi_0 &= \frac{c \sigma_T \dot{M}}{v_0 m_p \pi r_0^2}, \quad f_0 = \frac{\epsilon_0}{m_e c^2} \phi_0, \end{aligned} \quad (38)$$

the quantities D^\perp and D^\parallel are determined by expressions (16) and (17), respectively (the ratio D^\parallel/D^\perp will be varied). The quantity $\langle \sigma \rangle$ in calculations is supposed to be the geometrical mean of the values of cross-sections in the directions along and across the magnetic field.

The main computational problem is the solution (on each time step) of the eq. (25) (eq. (37)). Since the implicit alternating direction scheme (which was used, for example, in the work of Farinelli et al. (2012) for the case ‘1 spatial coordinate + photon energy’) in 3D case (‘2 spatial coordinates + photon energy’) is generally speaking unstable, it is possible to apply the locally 1D implicit scheme (Samarskii, A. A. 2001), which is based on the so-called method of summary approximation. However, this scheme is only conditionally stable in the case of considering equation (that can be shown, for example, with von Neumann method). The explicit schemes implying parallel computations can also be used. During the creation of this work in different time, both variants were being tested and used, depending on the exploited computational powers. The results presented here are achieved making use of the rectangular, equidistant in dimensionless variables meshes and the explicit scheme which includes the set of finite-difference operators corresponding to the original equation (37).

The approximation of the spatial diffusion terms can be performed making use of the distinct finite-difference pattern functionals for the calculation of the half-mesh value of the diffusion coefficient (Samarskii 1962). Here, the arithmetical mean is

used (so that $D_{i\pm 1/2}^{\perp,\parallel} = (D_i^{\perp,\parallel} + D_{i\pm 1}^{\perp,\parallel})/2$, i is the node number). For example, the operator of spatial diffusion along the magnetic field is expressed making use of the finite-difference pattern $h^{-2} (D_{i+1/2}^\parallel (\tilde{u}_{\xi, i+1} - \tilde{u}_{\xi, i}) - D_{i-1/2}^\parallel (\tilde{u}_{\xi, i} - \tilde{u}_{\xi, i-1}))$, where h is the mesh step.

The approximation of the diffusion terms is also possible after preliminary differentiation because of their continuity. In this variant, second derivatives are approximated by central tree-point patterns, and first derivatives in the terms $(\frac{\tilde{D}^\perp}{\tilde{r}} + \frac{\partial \tilde{D}^\perp}{\partial \tilde{r}}) \frac{\partial \tilde{u}_\xi}{\partial \tilde{r}}$ and $\frac{\partial \tilde{D}^\parallel}{\partial \tilde{z}} \frac{\partial \tilde{u}_\xi}{\partial \tilde{z}}$ are approximated by second-order central differences.

The second ξ derivative is approximated by a central tree-point pattern. The terms containing the first ξ derivatives are approximated making use of upwind differencing and accounting for general rules leading to the conditional stability of the scheme. The absence of computational instabilities is controlled during the converging over the entire computational domain.

3.3 Results

The resultant velocity distributions are shown (in terms of quantity Q for uniformity) in left panels of the Fig. 5 (for $\dot{M}_{17} = 1$) and Fig. 6 (for $\dot{M}_{17} = 2$). Simultaneously with 2D velocity profiles, the calculations lead to 2D profiles of the Compton temperature (7) displayed in Figs 5 and 6 (right panels) and to the sidewall emergent radiation spectra showed in Fig. 7, where the column sidewall spectral luminosity

$$L_\epsilon = 2\pi r_0 \int F_{\epsilon, r}(r_0, z) dz \quad (39)$$

is plotted for the different sets of problem parameters.

The obtained solutions for the velocity of the flow are in a very good conformity with the mound-like 2D shock structures obtained by solving the system including energy equation (10) (i.e., by solving eq. (18) in axially symmetrical case).

Each of the Figs 5 and 6 demonstrates the modifications in the shape of the front of the shock at fixed accretion rate that occur when the accretion column radius is varied at fixed D^\parallel (Figs 5a, b and Figs 6a, b) or when D^\parallel changes at fixed radius (Figs 5b, c and Figs 6b, c).

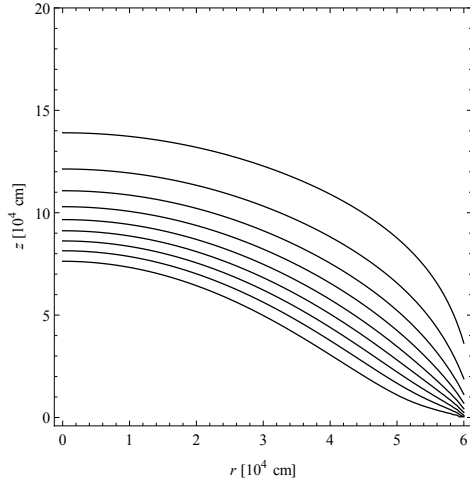
For the convenience, let each simulation (set of model parameters) be denoted by the number. At $\dot{M}_{17} = 1$: ‘1’ $D^\parallel = 10D^\perp$, $\tilde{r}_0 = 6$; ‘2’ $D^\parallel = 10D^\perp$, $\tilde{r}_0 = 8$; ‘3’ $D^\parallel = 4D^\perp$, $\tilde{r}_0 = 8$. At $\dot{M}_{17} = 2$: ‘4’ and ‘5’ $D^\parallel = 10D^\perp$, ‘6’ $D^\parallel = 4D^\perp$; the column radius is related with \dot{M} in each case as

$$\tilde{r}_0 = \tilde{r}_0|_{\dot{M}_{17}=1} \dot{M}_{17}^{1/7}. \quad (40)$$

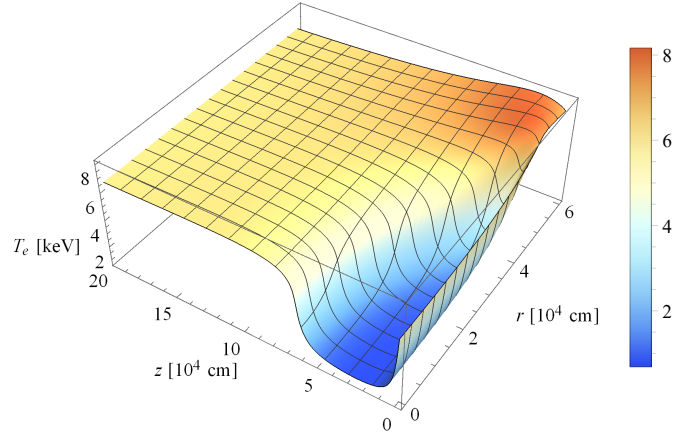
The temperature (7) is close to the electron one established in the area of the shock mainly by the Compton interaction with radiation at the time-scale (Zel’dovich & Levich 1970)

$$t_C \sim \frac{m_e c}{\sigma_T u}. \quad (41)$$

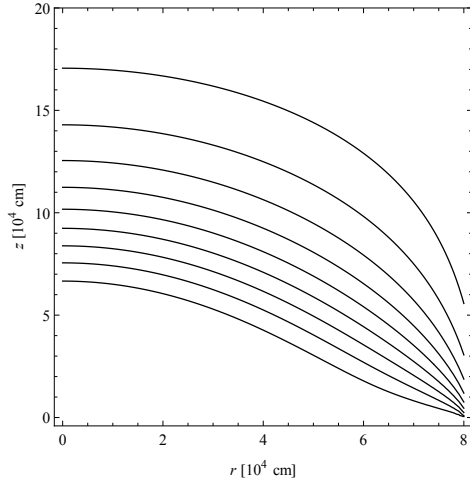
At a given r , the temperature has a minimum located in the settling zone under the shock (excluding the external radii where, in fact, this zone absents). That is in a qualitative (and quantitative, in the order of magnitude) agreement with the 1D profiles, presented by West et al. (2017a), (West et al. 2017b) (see plots for their T_{1C}). The distributions of the temperature (7) depend on the shock wave profile, so the value T_e changes in the radial direction for any fixed z (unless z does not significantly exceed the maximum shock height). The temperature value corresponding to the bottom boundary (independent of r) is dropped in the figures.



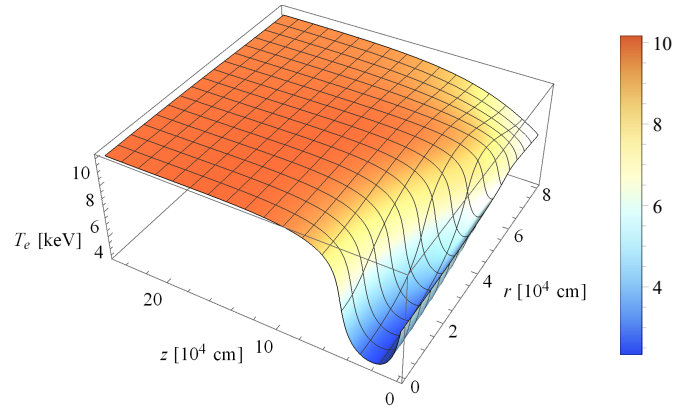
(a)



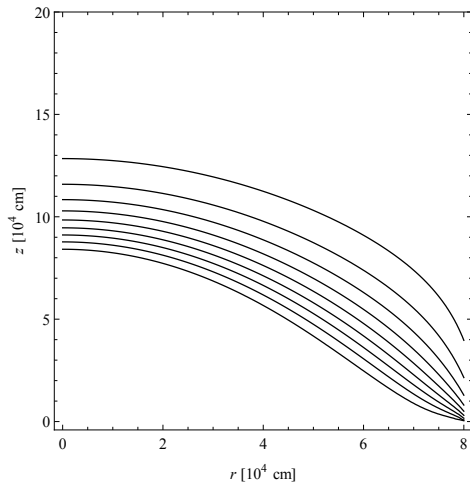
(d)



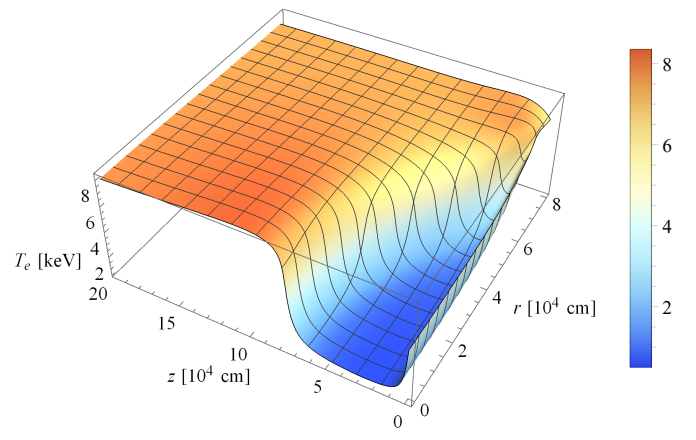
(b)



(e)



(c)



(f)

Figure 5. Contours of equal Q (from 0.9 to 0.1 with interval 0.1, from top to bottom) and profiles of the electron temperature (7) in the model of spatially 2D cylindrical accretion column, that are the result of self-consistent modelling for different sets of model parameters: ‘1’ (a, d), ‘2’ (b, e), ‘3’ (c, f).

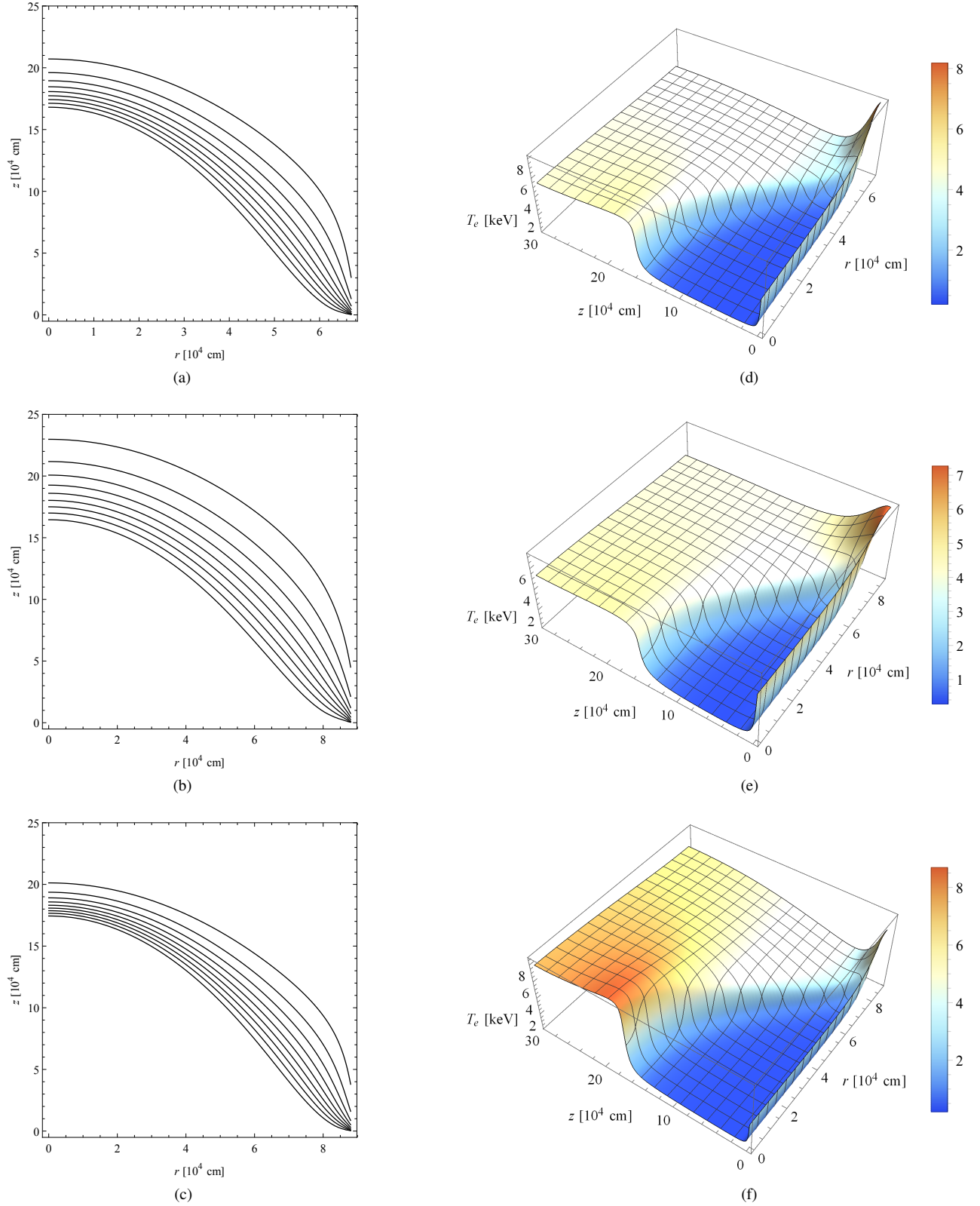


Figure 6. Same as Fig. 5, but for the mass accretion rate $\dot{M}_{17} = 2$, for different sets of model parameters: ‘4’ (a, d), ‘5’ (b, e), ‘6’ (c, f).

In the region of the shock, the time-scale (41) is significantly (by several orders of magnitude) less than both the time of diffusion of photons to the column boundary and the time of energy exchange between matter and radiation due to free-free processes. Thus, the local Compton equilibrium is a good approximation here. In the region that is external with respect to the shock, due to a decrease in the total radiation energy density, t_c begins to increase with increasing Q and becomes comparable with the mentioned time-scales. Therefore, only in this region, where $Q \simeq 1$, the electron temperature does not attain the values given by expression (7). However, the number of scattering events that photons undergo in this region is significantly less compared to the number of scatterings experienced in the shock wave, where the mean free path of photons is very short. Thus, one can believe that an overestimation of temperature above the shock does not significantly distort the effect of thermal Comptonization upon spectrum formation.

The current solutions (Fig. 7) demonstrate the dependence of the form of emerging radiation spectra on the magnitudes of velocity divergence and temperature in the shock. In the model under consideration, the temperature and the velocity are not independent and take on the values that provide an appropriate rate of the escape of photons from the column. It seems that a widening of the shock conditionates the increase of characteristic bulk Comptonization time-scale $(\nabla \cdot \mathbf{v})^{-1}$. In considering case, at fixed mass accretion rate (and at fixed D^+ and D^\parallel) this alteration is determined by the accretion column radius.

The increase of mass accretion rate up to the value $\dot{M}_{17} = 2$ leads to a narrowing of the shock and, consequently, to the growth of the value of the bulk Comptonization rate $\nabla \cdot \mathbf{v}$. The characteristic electron temperature slightly decreases with increasing \dot{M} (compare, for example, Figs 5d and 6d). In calculations ‘3’ and ‘6’ (Figs 5f and 6f), the temperature is practically invariable near the column axis.

The difference between the spectra at $\dot{M}_{17} = 1$ is not very pronounced, the maxima are at $\epsilon \simeq 20$ keV. The spectra ‘4’ and ‘6’ having the maxima at $\epsilon \simeq 9.5$ –10 keV remind the upper power-law solutions in fig. 1 of Lyubarskii & Syunyaev (1982) at high energies ($\epsilon \sim 10$ –50 keV), before the exponential cutoff. Meanwhile, the spectrum ‘5’ has a distinct maximum at $\epsilon \simeq 15$ keV.

There is also a qualitative agreement with the solutions of spatially 1D eq. (25) which have been obtained numerically by Farinelli et al. (2012) for the phenomenological power-law velocity profiles, $v \propto z^\eta$, where index η is one of the parameters of the problem. A decrease of η (flattening the velocity profile) leads to a hardening of spectrum tail at fixed column optical depth, electron temperature, and other parameters. This result was improved by Farinelli et al. (2016), where the additional terms have been introduced to the spatially 1D eq. (25) accounting approximately bremsstrahlung and sources of the fresh photons within the column volume. Nevertheless, the primary part of seed photons is generated under the neutron star surface, where free-free mechanisms play the essential role. Conversely, due to relations between the characteristic time-scales mentioned above, in the current approach, free-free interactions within the column are assumed not to be affected significantly on the radiation transfer in the shock wave, where the kinetic energy of the plasma flow is converted into radiation energy mainly via Compton mechanism.

In order to characterize the shape of the spectra shown in Fig. 7, the soft and hard X-ray colours (hardness ratios) determined by X-ray luminosity in specific energy bands as (e.g., Reig & Ne-

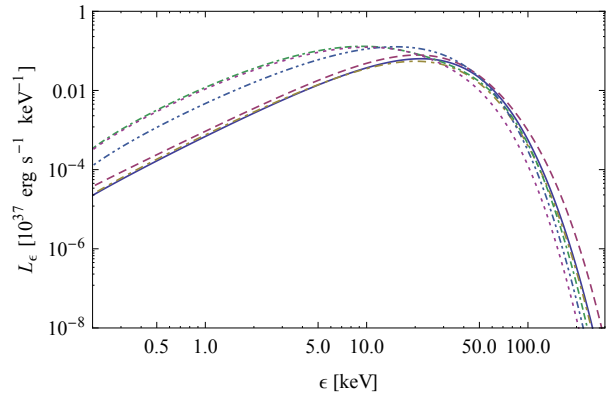


Figure 7. Spectra of radiation from sidewalls of the accretion columns, calculated simultaneously with velocity and temperature profiles plotted in Figs 5 and 6. The results correspond to different sets of the model parameters: ‘1’ (solid line), ‘2’ (dashed), ‘3’ (dot-dashed), ‘4’ (dot-double-dashed), ‘5’ (double-dot-dashed), ‘6’ (dotted).

Table 1. X-ray colours of the calculated spectra.

Spectrum (set of model parameters)	SC ₁	SC ₂	HC
1	1.88	37.05	3.87
2	1.88	36.78	3.68
3	1.82	33.68	3.55
4	1.21	12.01	1.89
5	1.51	20.74	2.64
6	1.24	12.49	1.87

spoli 2013)

$$SC_1 = \frac{L_{7-10 \text{ keV}}}{L_{4-7 \text{ keV}}}, \quad SC_2 = \frac{L_{5-12 \text{ keV}}}{L_{1-3 \text{ keV}}}, \quad HC = \frac{L_{15-30 \text{ keV}}}{L_{10-15 \text{ keV}}}, \quad (42)$$

have been calculated. The values are shown in Table 1 which demonstrates that the changes of the model parameters (including mass accretion rate) can lead to the variations of the hardness of spectrum of the direct column emission. At fixed D^\parallel , the spectrum becomes softer with increasing \dot{M} .

The radial component of spectral radiation flux calculated along the column sidewall, $F_{e,r}(r_0, z, \epsilon)$, is plotted in Fig. 8 for the cases of $\dot{M}_{17} = 1$ and $\dot{M}_{17} = 2$ corresponding to calculations ‘1’ and ‘4’. The maximal value of this quantity $\sim 10^{26} \text{ erg s}^{-1} \text{ cm}^{-2} \text{ keV}^{-1}$ holds for all simulations ‘1’–‘6’.

4 REMARKS AND CONCLUSIONS

The transition to 3D modelling is inevitably accompanied with increasing number of parameters of the problem, and only several particular results have been considered above. The numerical computations of Section 2 indicate the extent of the distinction of solutions from axially symmetric models and lead to the 2D asymmetric distributions of the flux over the surface of the column, which can be applied to the modelling of the observable pulse profiles of the emission of X-ray pulsars.

The height of the shock in the model of narrow unclosed hollow column is relatively small compared to the value in the filled-cylinder one. The radiation leaves the sidewalls predominantly near

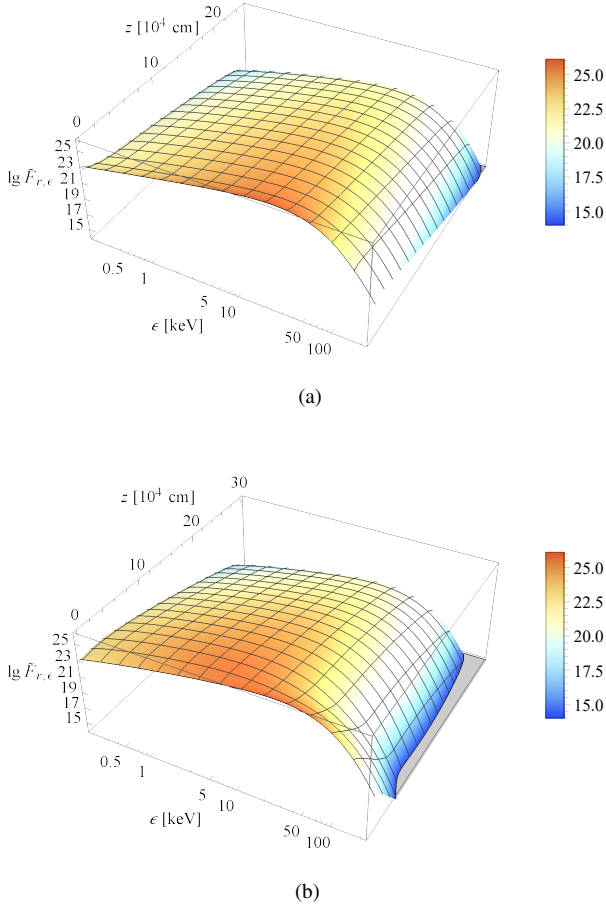


Figure 8. Spectral flux from the column sidewall plotted in the dependence on the height. Here, $\tilde{F}_{\epsilon, r} = F_{\epsilon, r}(r_0, z, \epsilon)/(\text{erg s}^{-1} \text{cm}^{-2} \text{keV}^{-1})$. The results correspond to simulations ‘1’ (a) and ‘4’ (b).

the neutron star surface independently of the geometry. The spectral distribution of this emission is determined by the solution of spectral-dependent problem which still contains the set of simplifications related mainly to using grey diffusion coefficients. Nevertheless, the results are important for a comparison of the column structure, resultant from the frequency-integral approaches (Davidson 1973, Postnov et al. 2015) and the results presented in the Section 3, containing, furthermore, 2D distribution of the electron temperature computed in the assumption of the local Compton equilibrium and the spectrum calculated in each point of the column. The conformity of solutions for the velocity signifies the correspondence of the obtained spectra to previous 2D shock models.

In the work of Lyubarskii & Syunyaev (1982) the shape of spectra was investigated in the dependence on the parameter related with the value of separability constant and hence with the rate of escape of photons from the column. Considering the spatially 1D kinetic equation, the authors are not interested in certain distribution of the occupation number over the emitting region surface, which is necessary for the accurate modelling of the beam of column emission. In the current work, it is shown that the equations lead to the exact 2D solution for the structure (within the framework of the model assumptions) simultaneously with the determination of T_e and the modelling of the spectral radiative transfer, without

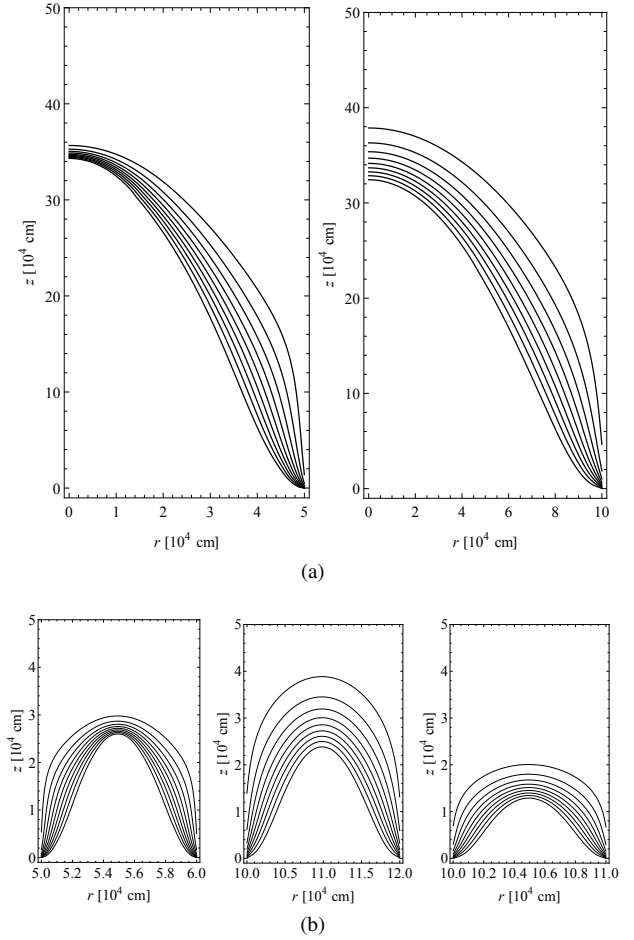


Figure 9. Contours of equal Q in 2D column models (from 0.9 to 0.1, from top to bottom with interval 0.1). Panels (a) show the solutions for the filled column at accretion rate $\dot{M}_{17} = 3$: $\tilde{r}_0 = 5$, left panel and $\tilde{r}_0 = 10$, right panel. Panels (b) show the solutions for the hollow column at accretion rate $\dot{M}_{17} = 5$. Left panel: $\tilde{r}_0 = 5$, $b = 0.2$; middle panel: $\tilde{r}_0 = 10$, $b = 0.2$; right panel: $\tilde{r}_0 = 10$, $b = 0.1$.

solving preliminary problems of determining the structure of the column.

It is clear that changing mass accretion rate may lead to significant modifications of the form of spectra at high energies $\epsilon > kT_e$ and variations in the soft hardness ratios as well.

In the frames of both approaches described in the current paper (cf. 2 and 3) the distribution of dimensionless velocity v/v_0 (or quantity Q) does not practically depend on the specific value of the velocity at the upper boundary (see Section 2). One can see that immediately from eq. (18) which includes the value of mass flux S .

In considering models, the shock height being measured, for example, along the column axis to the spatial middle of the transitional zone does not significantly depend on the column radius at fixed mass accretion rate. In the case of an axially symmetric ring-like column transverse section with inner radius r_0 , the height depends on the ratio b of thickness of the channel, br_0 , to r_0 , but also does not depend on the specific value of the radius. In order to show this numerically, and for higher accretion rates than considered above, let us adduce several solutions for the structure of axially symmetrical columns. These results are obtained by the numerical solution of equation (18) in cylindrical coordinates (2D

case). The boundary conditions consist with described in Section 2, and at the right boundaries, within the framework of both models, the condition for the radial component of radiation flux of type of condition (20) is set. At the axis of the filled column, $\partial u / \partial r = 0$. Fig. 9 indicates the modifications of the shock form for the filled column (a) and hollow column (b) (the values of \dot{M} are chosen from the reasons to illustrate all effects distinctly).

The mentioned statements correspond to simple analytic reasoning, described also by Mushtukov et al. (2015), Postnov et al. (2015). Actually, the equiparation of the radiation diffusion and matter settling times for the shock of height H indicates that $H \propto \dot{M}$ and $H \propto b\dot{M}$ for the filled and hollow-cylinder geometry, respectively. From Fig. 9, however, it follows that the dependence takes place also for the width of the shock (unaccounted for in the qualitative relations above) which rises with r_0 , when the pre-shock density of the flow (at constant v_0) decreases (see also Figs 5a, b and 6a, b). The shock width rises, moreover, with increasing D^\parallel (Figs 5b, c and 6b, c). In all calculations illustrated by Fig. 9, it is set that $D^\parallel = 10D^\perp$. Since the column radius depends on the magnetic field strength, such a property may be of interest in the framework of models implying a connection between variations in cyclotron resonance scattering feature energy with \dot{M} and changes of characteristic height of the shock.

ACKNOWLEDGEMENTS

I thank the anonymous reviewer for useful comments. This work was supported by RFBR according to the research project 18-32-00890 (development of self-consistent model) and the grant 17-15-506-1 of the Foundation for the advancement of theoretical physics and mathematics ‘BASIS’ (construction of the difference schemes underlying self-consistent modelling and creation of spatially three-dimensional models).

DATA AVAILABILITY

The calculations described in this paper were performed using the private codes developed by the author. The data presented in the figures are available on reasonable request.

REFERENCES

- Basko M. M., Sunyaev R. A., 1976, *MNRAS*, **175**, 395
 Becker P. A., Wolff M. T., 2007, *ApJ*, **654**, 435
 Blandford R. D., Payne D. G., 1981, *MNRAS*, **194**, 1033
 Canuto V., Lodenquai J., Ruderman M., 1971, *Phys. Rev. D*, **3**, 2303
 Davidson K., 1973, *Nature Physical Science*, **246**, 1
 Farinelli R., Ceccobello C., Romano P., Titarchuk L., 2012, *A&A*, **538**, A67
 Farinelli R., Ferrigno C., Bozzo E., Becker P. A., 2016, *A&A*, **591**, A29
 Gnedin I. N., Nagel W., 1984, *A&A*, **138**, 356
 Kompaneets A. S., 1956, *Zh. Eksp. Teor. Fiz.*, **31**, 876
 Lodenquai J., Canuto V., Ruderman M., Tsuruta S., 1974, *ApJ*, **190**, 141
 Lyubarskii Y. E., Syunyaev R. A., 1982, *Soviet Astronomy Letters*, **8**, 330
 Meszaros P., 1984, *Space Sci. Rev.*, **38**, 325
 Mushtukov A. A., Suleimanov V. F., Tsygankov S. S., Poutanen J., 2015, *MNRAS*, **447**, 1847
 Postnov K. A., Gornostaev M. I., Klochkov D., Laplace E., Lukin V. V., Shakura N. I., 2015, *MNRAS*, **452**, 1601
 Reig P., Nespoli E., 2013, *A&A*, **551**, A1
 Samarskii A. A., 1962, *Zh. Vychisl. Mat. Mat. Fiz.*, **2**, 25

- Samarskii, A. A. 2001, The theory of difference schemes. Marcel Dekker, inc., New York, Base
 Wang Y.-M., Frank J., 1981, *A&A*, **93**, 255
 West B. F., Wolfram K. D., Becker P. A., 2017a, *ApJ*, **835**, 129
 West B. F., Wolfram K. D., Becker P. A., 2017b, *ApJ*, **835**, 130
 Zel’dovich Y. B., Levich E. V., 1970, *Soviet Journal of Experimental and Theoretical Physics Letters*, **11**, 35